the FEBS Journal

pH modulates the binding of early growth response protein 1 transcription factor to DNA

David C. Mikles, Vikas Bhat, Brett J. Schuchardt, Brian J. Deegan, Kenneth L. Seldeen, Caleb B. McDonald and Amjad Farooq

Department of Biochemistry & Molecular Biology, Leonard Miller School of Medicine, University of Miami, FL, USA

Keywords
histidine protonation; intracellular pH; protein dynamics; protein–DNA thermodynamics; zinc fingers

Correspondence
A. Farooq, Department of Biochemistry & Molecular Biology, Leonard Miller School of Medicine, University of Miami, Miami, FL 33136, USA
Fax: +1 305 243 3955
Tel: +1 305 243 2429
E-mail: amjad@farooqlab.net

(Received 5 November 2012, revised 21 May 2013, accepted 28 May 2013)

doi:10.1111/febs.12360

The transcription factor early growth response protein (EGR)1 orchestrates a plethora of signaling cascades involved in cellular homeostasis, and its downregulation has been implicated in the development of prostate cancer. Herein, using a battery of biophysical tools, we show that the binding of EGR1 to DNA is tightly regulated by solution pH. Importantly, the binding affinity undergoes an enhancement of more than an order of magnitude with an increase in pH from 5 to 8, implying that the deprotonation of an ionizable residue accounts for such behavior. This ionizable residue is identified as His382 by virtue of the fact that its replacement by nonionizable residues abolishes the pH dependence of the binding of EGR1 to DNA. Notably, His382 inserts into the major groove of DNA, and stabilizes the EGR1–DNA interaction via both hydrogen bonding and van der Waals contacts. Remarkably, His382 is mainly conserved across other members of the EGR family, implying that histidine protonation–deprotonation may serve as a molecular switch for modulating the protein–DNA interactions that are central to this family of transcription factors. Collectively, our findings reveal an unexpected but a key step in the molecular recognition of the EGR family of transcription factors, and suggest that they may act as sensors of pH within the intracellular environment.

Introduction

The transcription factor early growth response protein (EGR)1, also known as Zif268, bolsters the classic TA–DB modular architecture, where TA is the N-terminal transactivation domain and DB is the C-terminal DNA-binding domain. Such a modular design is exquisitely suited for the role of EGR1 in coupling extracellular stimuli such as hormones, neurotransmitters and growth factors to changes in gene expression that are responsible for a myriad of cellular activities, ranging from cell growth and proliferation to apoptosis and oncogenic transformation [1–4]. Importantly, cellular expression of EGR1 is downregulated in glioblastomas, lymphomas, and cancers of the lung and breast [5–8], implying that EGR1 plays a tumor-suppressive role in various cancers. This view is further supported by the observation that tumor suppressors such as PTEN, p53 and transforming growth factor-β are direct targets of EGR1 [9–11]. Paradoxically, expression of EGR1 is upregulated in prostate tumors [12–16], implying that the role of EGR1 is tissue-dependent, and that it probably serves as a double-edged sword, depending on the biological context.

Abbreviations
DB_H382A, DNA-binding domain containing the H382A substitution; DB_H382E, DNA-binding domain containing the H382E substitution; DB_H382K, DNA-binding domain containing the H382K substitution; DB_H382R, DNA-binding domain containing the H382R substitution; DB_HH, DNA-binding domain containing the E354H/E410H double substitution; DB_WT, wild-type DNA-binding domain; DB, DNA-binding domain; EGR, early growth response protein; ITC, isothermal titration calorimetry; KLF, Krueppel-like factor; MD, molecular dynamics; rmsf, root mean square fluctuation; TA, transactivation domain; ZF, zinc finger; ZRE, Zif268 (EGR1) response element.

Regardless of the complexity of the physiological actions of EGR1, it primarily exerts its effects by virtue of its ability to bind to the promoters of target genes containing the GCGTGGGCG consensus motif, referred to hereinafter as the Zif268 response element (ZRE), in a sequence-dependent manner. The EGR1–DNA interaction is driven by the binding of DB as a monomer to the major groove within the ZRE duplex [17]. This mode of DNA binding is somewhat unusual, in that transcription factors usually recognize their promoter elements either as homodimers or as heterodimers. However, DB of EGR1 is composed of three tandem copies of C2H2-type zinc fingers (ZFs), designated herein ZFI, ZFII, and ZFIII, which assemble into an arc-shaped architecture that snugly fits into the major groove of DNA (Fig. 1A). Importantly, each ZF within DB contains an α-helix and an antiparallel double-stranded (β1–β2) β-sheet that, together, sandwich a Zn^{2+}, the latter being coordinated in a tetrahedral arrangement by two histidines and two cysteines. Remarkably, the EGR1–DNA interaction is driven by the binding of each ZF to one of the three subsites, each subsite being composed of a trinucleotide sequence, within the 9-bp GCGTGGGCG consensus motif (Fig. 1B). The three ZFs within DB thus act as a cooperative unit and bind to their cognate DNA in a manner akin to the cooperativity observed between monomeric units of dimeric transcription factors. In particular, at each of the three subsites within the ZRE duplex occupied by one of the three ZFs, the protein–DNA contacts are largely afforded by the α-helix, which fits into the major groove of DNA, and the β2-strand, which contacts the DNA phosphate backbone (Fig. 1A). Notably, the β1-strand appears to play a scaffolding role, and makes no discernible contacts with DNA.

Of particular note is the observation that the binding DB of EGR1 appears to be strongly governed by numerous van der Waals contacts in addition to an extensive network of intermolecular hydrogen bonding and ion pairing [17]. Ironically, detailed examination of the atomic structure of DB of EGR1 in complex with the ZRE duplex shows that a histidine (His382), located within the first turn of the α-helix (αII) of ZFII but not involved in coordinating the zinc ligand, protrudes deep into the major groove at the protein–DNA interface (Fig. 1A). It should be noted that the imidazole ring of His382 is coplanar with G0 and stacks against the pyrimidine ring of T1 within the ZRE duplex. Importantly, the His382–G0 interaction appears to be stabilized via a two-prong mechanism: first, the coplanar alignment of the imidazole ring of His382 and the purine ring of G0, the central guanine of the middle trinucleotide subsite that accommodates ZFII within DB, facilitates the formation of a hydrogen bond between the Hε2 atom of His382 and the N7 atom of G0; and second, stacking of the imidazole ring of His382 against the pyrimidine ring of T1 promotes van der Waals contacts between the protein and DNA. Given that the pK_a values of histidines located within the binding and catalytic centers of proteins are frequently perturbed [18,19], we wondered whether protonation–deprotonation of His382 may be involved in modulating EGR1–DNA interactions in response to changes in solution pH. Importantly, His382 located within ZFII is replaced by a glutamate in ZFI (Glu354) and ZFIII (Glu410) at the structurally equivalent positions. Such a lack of conservation of His382 in ZFI and ZFIII implies a unique role of ZFII in dictating the binding of EGR1 to DNA.

In an attempt to test our hypothesis that the protonation–deprotonation of His382 may be involved in modulating EGR1–DNA interactions, we analyzed the pH dependence of the binding of DB of EGR1 to a 15-mer dsDNA oligonucleotide containing the ZRE motif, using various biophysical tools. Our study shows that the binding of EGR1 to DNA is tightly regulated by solution pH, by virtue of the ability of His382 to undergo protonation–deprotonation. Remarkably, His382 is mainly conserved across other members of the EGR family, implying that histidine protonation–deprotonation may serve as a molecular switch for modulating the protein–DNA interactions that are central to this family of transcription factors. Collectively, our findings reveal an unexpected but a key step in the molecular recognition of the EGR family of transcription factors, and suggest that they may act as sensors of pH within the intracellular environment.

Results and Discussion

Protonation–deprotonation of His382 modulates the binding of EGR1 to DNA

In an attempt to test our hypothesis that His382 within EGR1 may be subject to protonation–deprotonation equilibrium, we measured the effect of varying solution pH values, ranging from 5 to 8, on the binding of the ZRE duplex to wild-type DB (DB_WT) of EGR1, using isothermal titration calorimetry (ITC) (Fig. 2; Table 1). Our data show that the binding of DB_WT to DNA is strongly pH dependent. Thus, whereas DB-WT binds to DNA with an affinity close to 2 μM at pH 5, the binding increases by more than an order of magnitude to ~ 150 nM at pH 8 (Table 1).

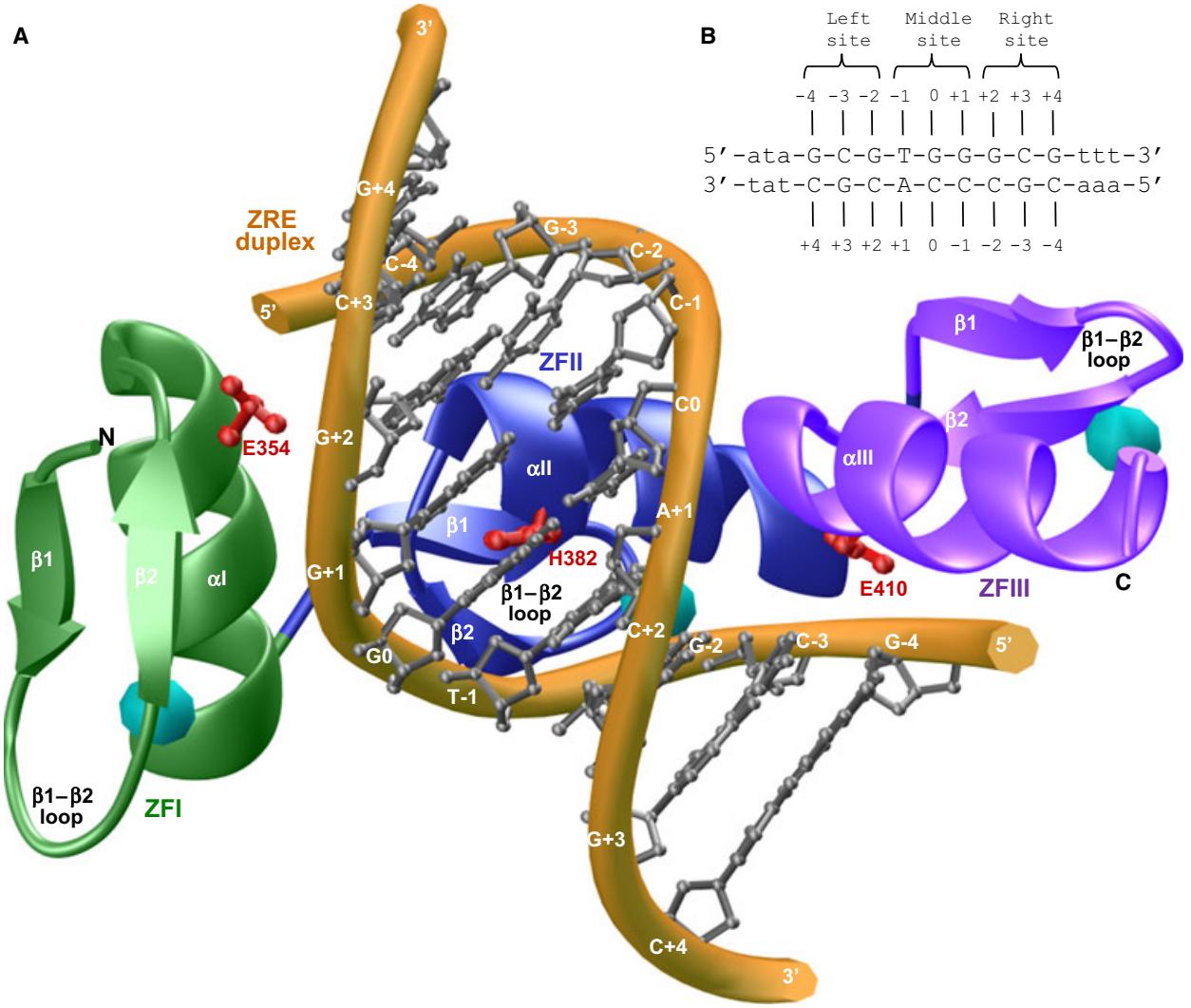

Fig. 1. Protein and DNA analysis. (A) Structural model of DB (residues 336–420) of human EGR1 in complex with the ZRE duplex containing the GCGTGGGCG consensus sequence. Note that DB is composed of three tandem C2H2-type ZFs, designated ZFI (green), ZFII (blue), and ZFIII (magenta). Each ZF is composed of an α-helix and a double-stranded (β1–β2) antiparallel β-sheet that, together, sandwich a Zn^{2+}, indicated by a sphere (cyan). In each ZF, the Zn^{2+} is coordinated by two histidines and two cysteines in a tetrahedral arrangement. The DNA backbone is shown in yellow, and the bases are shown in gray for clarity. Note also that each ZF recognizes a triplet of bases within the 9-bp GCGTGGGCG consensus sequence. The side chain moieties of Glu354 (ZFI), His382 (ZFII) and Glu410 (ZFIII) within DB that contact DNA are shown in red. (B) The duplex containing the GCGTGGGCG tripartite consensus motif. The consensus nucleotides within this motif are in upper case, and the flanking nucleotides are shown in lower case. The three subsites within the consensus motif are marked for clarity, and accommodate ZFI (right site), ZFII (middle site) and ZFIII (left site) within DB. The numbering of various nucleotides with respect to the central nucleotide of the middle site (which is arbitrarily assigned zero) is indicated.

This finding strongly implies that the protonation of an ionizable residue with a pK_a close to neutral pH most likely accounts for such enhancement in the binding of DB to DNA. To test our hypothesis that His382 serves as the site for such protonation–deprotonation, we next measured the effect of the binding of DB containing the H382A substitution (DB_H382A) to DNA. We expected that the H382A substitution would remove the contribution of the ionizable imidazole moiety of His382, and thereby eliminate the pH dependence of the binding of DB to DNA. Consistent with this rationale, our comparative analysis revealed that, whereas the binding of DB_WT to DNA monotonically increased as a function of pH, the binding of DB_H382A showed no dependence on solution pH (Fig. 3).

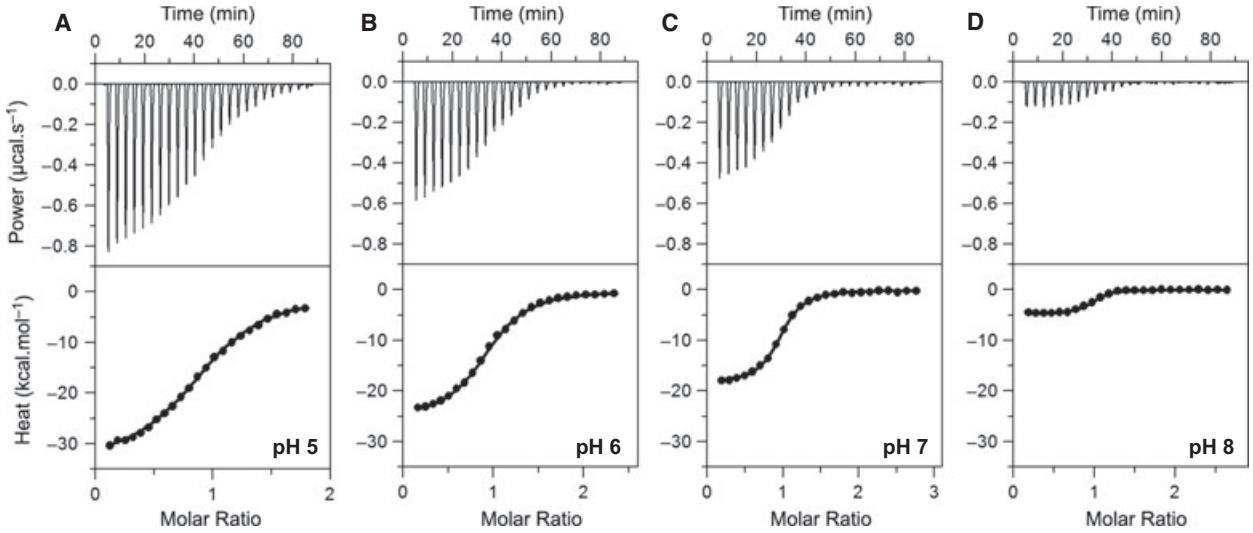

Fig. 2. Representative ITC isotherms at 25 °C for binding of the ZRE duplex to DB_WT of EGR1 at pH 5 (A), pH 6 (B), pH 7 (C), and pH 8 (D). The upper panels show raw ITC data expressed as change in thermal power with respect to time over the period of titration. In the lower panels, change in molar heat is expressed as a function of molar ratio of the ZRE duplex to DB. The solid lines in the lower panels show the fit of data to a one-site model, as shown in Eqn (1), with MICROCAL ORIGIN software.

Table 1. Thermodynamic parameters for binding of the ZRE duplex to DB_WT of EGR1 at various pH values. The binding stoichiometries for the fits agreed to within ±10%. Errors were calculated from at least three independent measurements. All errors are given to one standard deviation.

pH	K_d (nM)	ΔH (kcal·mol^{-1})	$T\Delta S$ (kcal·mol^{-1})	ΔG (kcal·mol^{-1})
5.0	1962 ± 485	−33.43 ± 0.73	−25.63 ± 0.58	−7.80 ± 0.15
5.5	2045 ± 363	−31.01 ± 0.68	−23.23 ± 0.57	−7.77 ± 0.11
6.0	806 ± 77	−25.26 ± 0.30	−16.94 ± 0.25	−8.32 ± 0.06
6.5	311 ± 30	−22.49 ± 0.65	−13.60 ± 0.70	−8.89 ± 0.06
7.0	236 ± 27	−18.71 ± 0.46	−9.67 ± 0.39	−9.05 ± 0.07
7.5	186 ± 16	−14.34 ± 0.31	−5.15 ± 0.25	−9.19 ± 0.05
8.0	149 ± 15	−4.53 ± 0.34	+4.80 ± 0.28	−9.32 ± 0.06

To provide further support for our hypothesis, we also measured the effect of the binding of DB containing the H382K (DB_H382K) and H382R (DB_H382R) substitutions to DNA. These substitutions were introduced to mimic the effect of a protonated histidine containing a net positive charge at His382. As expected, the binding of neither DB_H382K nor DB_H382R to DNA showed pH dependence (Fig. 3). However, both DB_H382K and DB_H382R bound to DNA with affinities similar to those observed for the binding of DB_WT at pH 5 rather than its enhanced binding at pH 8 (Tables 1 and 2). We believe that this is most likely attributable to the fact that, whereas Lys382 and Arg382 may carry a net positive charge in a manner akin to protonated His382, their nonaromatic side chain moieties do not structurally resemble the imidazole ring of His382, and are therefore unlikely to completely substitute for its ability to engage in close intermolecular contacts with the DNA. Given that His382 located within ZFII of DB is replaced by a glutamate at the structurally equivalent positions within ZFI (Glu354) and ZFIII (Glu410) (Fig. 1A), we also wondered how the H382E substitution might influence the binding of DB to DNA. To investigate this, we measured the effect of the binding of DB containing the H382E substitution (DB_H382E) to DNA. Consistent with our hypothesis that His382 is responsible for the pH-dependent binding of DB to DNA, our data revealed that the binding of DB_H382E to DNA was independent of solution pH (Fig. 3). Prompted by this promising observation, we next wondered how the E354H and E410H substitutions might affect the binding of DB to DNA. To investigate this, we measured the effect of the binding of DB containing the E354H/E410H double substitution (DB_HH) to DNA.

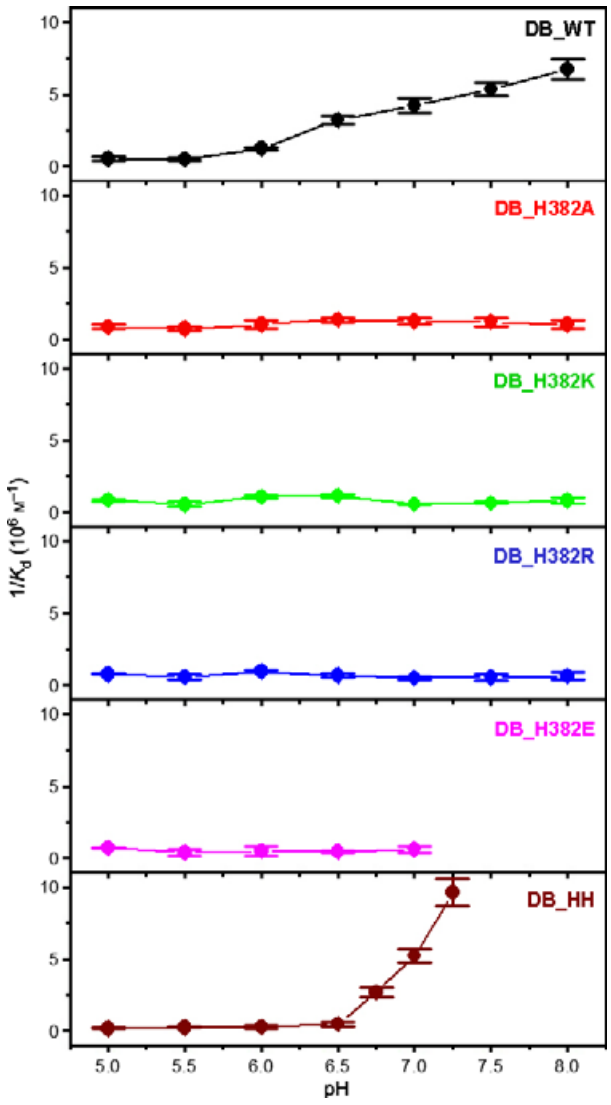

Fig. 3. Dependence of $1/K_d$ on pH for binding of the ZRE duplex to DB_WT (black), DB_H382A (red), DB-H382K (green), DB_H382R (blue), DB_H382E (magenta) and DB_HH (brown) of EGR1 at 25 °C. The error bars were calculated from at least three independent measurements to one standard deviation.

Remarkably, the binding of DB_HH to DNA showed even stronger pH dependence than that observed for DB_WT (Fig. 3). Thus, whereas the binding of DB_WT to DNA showed an eight-fold increase in affinity as the solution pH was raised from a 5 to 7, DB_HH showed an approximately 30-fold enhancement over the same pH range (Tables 1 and 3). Taken together, these observations unequivocally demonstrate that the protonation–deprotonation of His382 accounts for the binding of EGR1 to DNA in a pH-dependent manner.

It is also noteworthy that the enthalpic change associated with the binding of DB_WT to the ZRE duplex was observed to be independent of the ionization enthalpy of reaction buffers such as phosphate and Tris. This implies that the protonation–deprotonation of His382 in EGR1 is solely dependent upon solution pH, and that it is not coupled to DNA binding. Given that the protonation of His382 hampers the binding of EGR1 to DNA, the lack of such proton-coupled equilibrium for DNA binding would indeed be thermodynamically unfavorable and thus highly undesirable. In short, our data strongly suggest that the solution pH is likely to play a key regulatory role in fine-tuning the binding of EGR1 to DNA under physiological conditions within the living cell.

Binding of EGR1 to DNA is enthalpy–entropy-compensated

In addition to the demonstration that the solution pH modulates the binding of EGR1 to DNA, our data also shed light on the underlying thermodynamics governing this key protein–DNA interaction (Fig. 4; Table 1). Interestingly, whereas enthalpy drives the EGR1–DNA interaction accompanied by opposing entropic forces in the physiological pH range, the enthalpic contributions appear to monotonically decrease with an increase in pH from 5 to 8 (Fig. 4A). Noting that enthalpic contributions most likely result from favorable intermolecular hydrogen bonding, ion pairing, and van der Waals forces, the most straightforward interpretation of this finding is that increasing pH disrupts or mitigates the effect of such intermolecular forces on protein–DNA interactions. On the other hand, the entropic contributions to the free energy become more favorable with increasing pH (Fig. 4B). Such a loss of opposing entropic change most probably results from the change in the interactions of water molecules with protein and DNA with increasing solution pH. It is noteworthy that the release of hydrogen-bonded and trapped water within the crevices and cavities in protein and DNA is a major contributor to the favorable entropic change upon association. Accordingly, the changes in solution pH would directly affect the equilibrium between bulk water and trapped water, and thereby the entropic contributions to the overall free energy. Notably, the loss of enthalpic contributions is more or less compensated for by an equal but opposite favorable increase in entropic contributions, such that there is little or no net gain in the overall free energy (Fig. 4A,B). This reciprocal relationship between enthalpy and entropy can be explained by the enthalpy–entropy compensation phenomenon [20–24].

Table 2. Thermodynamic parameters for binding of the ZRE duplex to DB_WT and various mutant constructs of DB of EGR1 at pH 7.0. The binding stoichiometries for the fits agreed to within ± 10%. Errors were calculated from three independent measurements. All errors are given to one standard deviation.

	K_d (nM)	ΔH (kcal·mol^{-1})	$T\Delta S$ (kcal·mol^{-1})	ΔG (kcal·mol^{-1})
DB_WT	236 ± 27	−18.71 ± 0.46	−9.67 ± 0.39	−9.05 ± 0.07
DB_H382A	812 ± 137	−14.34 ± 0.69	−6.02 ± 0.58	−8.32 ± 0.10
DB_H382K	1759 ± 160	−5.20 ± 0.37	+2.66 ± 0.31	−7.86 ± 0.05
DB_H382R	1901 ± 235	−6.98 ± 0.22	+0.84 ± 0.14	−7.81 ± 0.07
DB_H382E	1492 ± 237	−2.34 ± 0.14	+5.62 ± 0.23	−7.96 ± 0.10
DB_HH	192 ± 18	−5.43 ± 0.20	+3.75 ± 0.26	−9.17 ± 0.06

Table 3. Thermodynamic parameters for binding of the ZRE duplex to DB_HH of EGR1 at various pH values. The binding stoichiometries for the fits agreed to within ± 10%. Errors were calculated from at least three independent measurements. All errors are given to one standard deviation.

pH	K_d (nM)	ΔH (kcal·mol^{-1})	$T\Delta S$ (kcal·mol^{-1})	ΔG (kcal·mol^{-1})
5.0	5456 ± 1079	−21.39 ± 0.61	−14.20 ± 0.50	−7.19 ± 0.12
5.5	3860 ± 645	−20.39 ± 0.40	−12.99 ± 0.29	−7.40 ± 0.10
6.0	3736 ± 1076	−14.87 ± 0.57	−7.45 ± 0.74	−7.42 ± 0.17
6.5	2177 ± 696	−9.37 ± 0.33	−1.63 ± 0.14	−7.75 ± 0.19
7.0	192 ± 18	−5.57 ± 0.20	+3.75 ± 0.14	−9.17 ± 0.06

Indeed, as shown in Fig. 4C, the binding of EGR1 to DNA as a function of pH is in agreement with this enthalpy–entropy compensation phenomenon.

Neutral pH has little effect or a negligible effect on the structure of DB of EGR1

Given that the binding of EGR1 to DNA is tightly regulated by pH, we next analyzed the extent to which pH may also affect the secondary structure and stability of DB_WT, using far-UV CD (Fig. 5). Our analysis revealed that the far-UV CD spectral features of DB_WT are characterized by a positive band centered around 195 nm and a negative band centered around 208 nm, with a shoulder at 225 nm (Fig. 5A). These observations are consistent with the αβ-fold of the DB. Importantly, whereas increasing the solution pH from 5 to 6 appeared to enhance the spectral intensity of DB_WT in the 200–240-nm region, there was little effect or a negligible effect on the spectral intensity as the pH was further raised from 6 to 8. This implies that, whereas pH below 6 significantly compromises the structural integrity of DB_WT, its secondary structure undergoes little or no change in the pH range from 6 to 8. Next, to test how changes in secondary structure affect the stability of DB, we probed the dependence of mean ellipticity observed at a wavelength of 222 nm, $[\theta_{222}]$, as a function of pH, over the temperature range 20–100 °C, using far-UV CD (Fig. 5B). In striking contrast to the findings of our secondary structural analysis above, our thermal scans suggested that DB_WT has a melting temperature (T_m) of ~ 55 °C under all pH conditions from 5 to 8. This finding argues that, whereas acidic pH may destabilize the secondary structure of DB_WT, such a loss of structure does not necessarily translate into lower thermal stability. Collectively, our far-UV CD analysis shows that, whereas solution pH in the range from 6 to 8 significantly enhances the binding affinity of DB for its cognate DNA, by virtue of the ability of His382 to undergo protonation–deprotonation, it has little effect or a negligible effect on its secondary structure and thermal stability. However, it should be borne in mind that far-UV CD is a bulk technique that probes the overall global average structure, rather than providing information on specific regions or residues, which may undergo structural fluctuations in a transient manner. Accordingly, our far-UV CD analysis presented above may have overlooked the effect of solution pH on the structure of DB at the atomic level.

Protonation of His382 compromises thermodynamic contacts at the protein–DNA interface

In order to rationalize the effect of protonation of His382 on electrostatics at the protein–DNA interface, we generated electrostatic surface potential maps of DB containing His382 in the unprotonated and

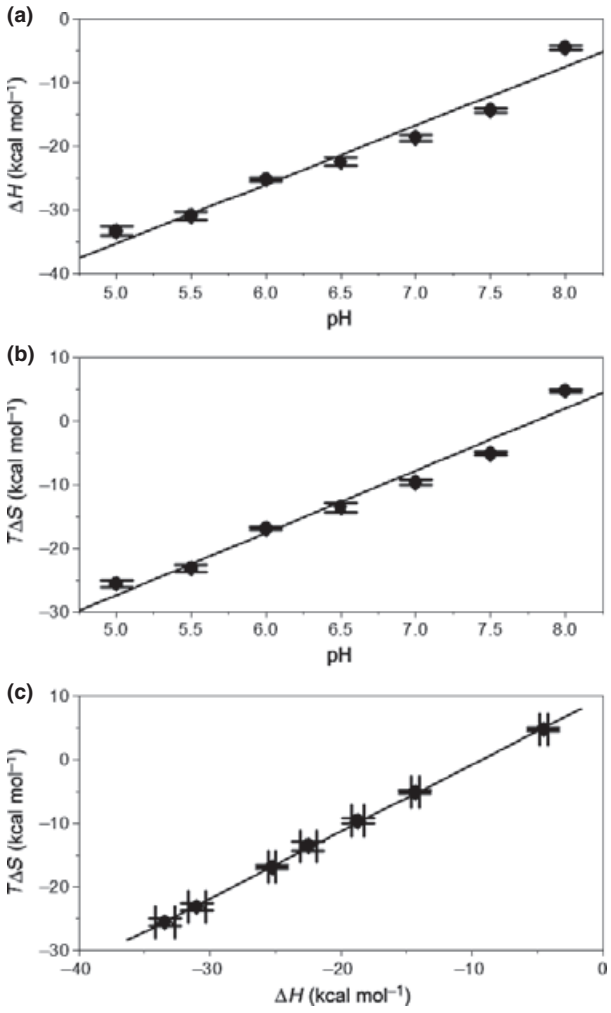

Fig. 4. Dependence of thermodynamics on pH for binding of the ZRE duplex to DB_WT of EGR1 at 25 °C. (A) ΔH–pH plot. (B) $T\Delta S$–pH plot. (C) $T\Delta S$–ΔH plot. The error bars were calculated from at least three independent measurements to one standard deviation.

protonated state in complex with the ZRE duplex (Fig. 6). Our data provide interesting insights into how such protonation transforms the electrostatic polarization of the protein surface at His382, so as to render its contact with DNA less thermodynamically favorable. In the unprotonated state, His382 occupies what appears to be a largely apolar surface that is destined to engage in close van der Waals contacts with DNA by virtue of the ability of the imidazole ring of His382 to stack against the pyrimidine ring of T1 (Fig. 6A). Such stacking also results in the coplanar alignment of the imidazole ring of His382 and the purine ring of G0, and thereby facilitates the formation of a hydrogen bond between the Hε2 atom of His382 and the N7 atom of G0. Importantly, upon protonation of the Nδ1 atom of His382, the local surface becomes positively charged (Fig. 6B). Such a scenario would compromise the ability of His382 to engage in intermolecular hydrogen bonding and van der Waals contacts with DNA, and thereby eliminate an important thermodynamic component contributing to the free energy driving EGR1–DNA interactions. Accordingly, the unfavorable interactions of the protonated state as compared with unprotonated state of His382 would weaken protein–DNA contacts, in agreement with our demonstration that increasing pH enhances EGR1–DNA interactions. In short, the aforementioned electrostatic surface potential maps of DB strongly suggest that the protonation of His382 would result in the loss of favorable thermodynamic factors that would facilitate the two molecular surfaces coming into close proximity to achieve a tight molecular fit.

Protonation of His382 mitigates structural stability and alters protein–DNA dynamics

Our analysis presented above suggests strongly that the protonation of His382 serves as a molecular switch in modulating EGR1–DNA interactions. To probe the effect of such protonation on protein stability and dynamics at the atomic level, we next conducted molecular dynamics (MD) simulations on DB containing His382 in the unprotonated and protonated state in complex with the ZRE duplex (Fig. 7). As shown in Fig. 7A, the MD trajectories reveal that, whereas the unprotonated state reaches structural equilibrium after ~ 20 ns, with an overall rmsd of ~ 1.5 Å, its structural stability is somewhat compromised upon protonation, with an rmsd of > 2.0 Å. This observation suggests that the protonation of His382 most likely destabilizes protein–DNA contacts, in agreement with our analysis presented above. Although the overall global changes in protein dynamics between the protonated and unprotonated forms of DB may not appear to be very drastic, close inspection of how protonation affects the dynamics of the αII helix (harboring His382) within ZFII of DB is revealing. Thus, whereas the average rmsd per residue for the αII helix is close to 0.2 Å within the unprotonated form of DB, it appears to hover around 1.5 Å within the protonated form (Fig. 7B). This salient observation suggests strongly that, whereas the αII helix is highly ordered in the unprotonated form of DB, protonation of His382 results in substantial disorder. In agreement with our thermodynamic data presented above, we believe that such order–disorder transition of the αII helix upon protonation of His382 severely compromises the

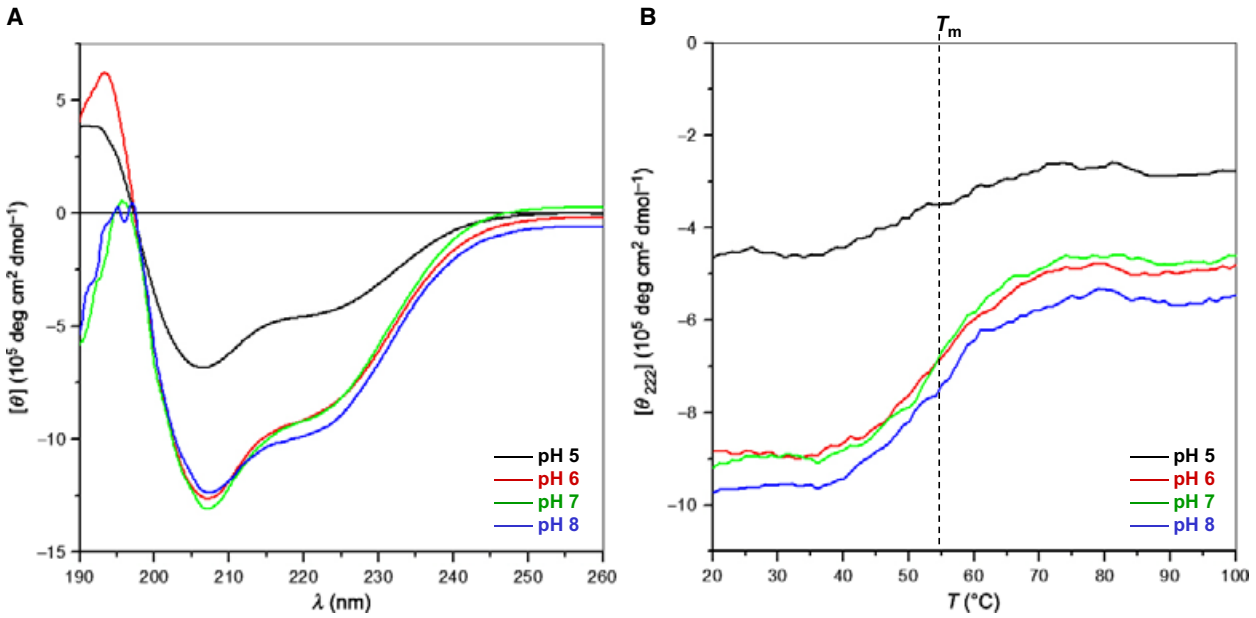

Fig. 5. Far-UV CD analysis of DB_WT of EGR1 at pH 5 (black), pH 6 (red), pH 7 (green) and pH 8 (blue). (A) Representative far-UV spectra as a function of pH over the wavelength (λ) range 190–260 nm at 25 °C. (B) Representative melting curves as a function of pH over the temperature (T) range 20–100 °C expressed in terms of the mean ellipticity observed at a wavelength of 222 nm, [θ_{222}]. Note that the vertical dashed line indicates the melting transition (T_m) of the curves.

protein–DNA contacts, resulting in the loss of high-affinity binding.

An alternative means to assess the mobility and stability of macromolecular complexes is through an assessment of the root mean square fluctuation (rmsf) of specific atoms over the course of MD simulation. In Fig. 7C, we show such an analysis for the backbone atoms of each residue within DB. The rmsf analysis reveals that, whereas a majority of residues within DB appear to be well ordered in both the unprotonated and the protonated state, there are subtle differences within the loop regions. Thus, for example, residues within the β1–β2 loop of ZFI show similar mobilities between the protonated and unprotonated state. In sharp contrast, the mobility of residues in the β1–β2 loop of ZFII is markedly greater in the unprotonated state than in the protonated state, whereas the opposite trend is observed for the residues in the β1–β2 loop of ZFIII. Additionally, residues located within the C-terminus of the αIII helix of ZFIII appear to show much greater mobility than the corresponding residues in ZFI and ZFII. This implies that protonation of His382 located within ZFII affects protein dynamics not only locally but also globally, stretching across all three ZFs. Accordingly, this finding suggests that the three ZFs most likely bind to DNA in a cooperative manner, and that such allosteric communication is most likely transmitted through protein dynamics, rather than structural changes. Of particular note is the observation that residues 380–390 spanning the αII helix show substantially higher fluctuations in the protonated form of DB than in the unprotonated form (Fig. 7D). This further supports the notion that protonation of His382 results in order–disorder transition of the αII helix.

Protonation of His382 affects the structural integrity of the αII helix

In an attempt to shded further light on how protonation of His382 affects the dynamics of the αII helix located within ZFII of DB, we analyzed how MD simulations affect its secondary structural features (Fig. 8). Notably, protonation of His382 results in a dramatic loss of the propensity of residues 380–390 spanning the αII helix to adopt an α-helical conformation, particularly those located within the N-terminal and C-terminal regions (Fig. 8A). Equally importantly, the loss of such helicity within the αII helix exquisitely correlates with changes in the backbone torsion angles ϕ and ψ (Fig. 8B). Thus, whereas residues spanning the αII helix within the unprotonated form adopt, respectively, ϕ and ψ torsion angles of approximately −65° and −40° (characteristic of an ideal α-helix on the Ramachandran plot), the ϕ and ψ angles in the protonated form, respectively, adopt values of

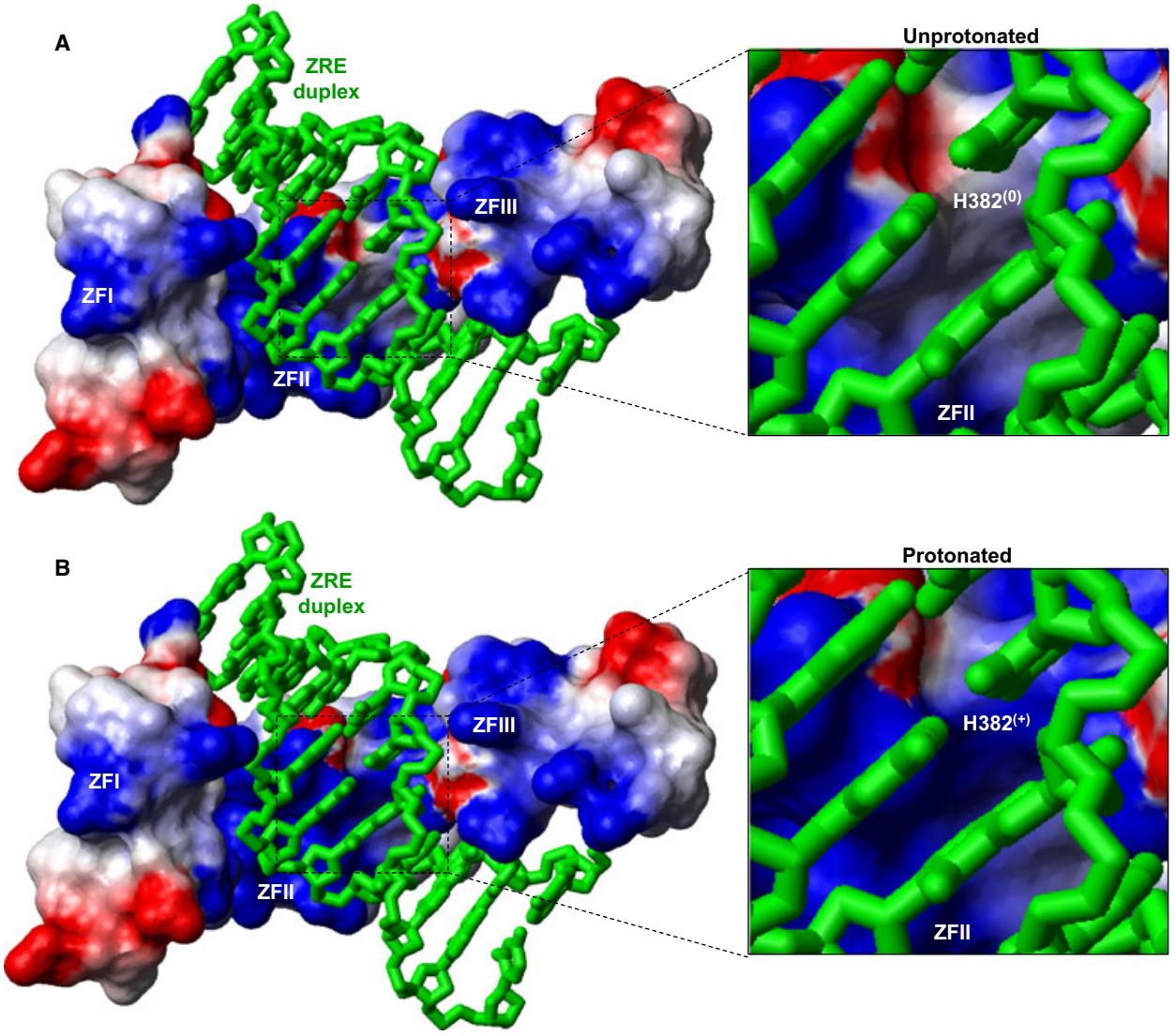

Fig. 6. Electrostatic surface potential maps of the structural models of DB_WT of EGR1 containing His382 in the unprotonated (A) and protonated (B) forms in complex with the ZRE duplex. Note that, in the unprotonated form, His382 is protonated only at the Nε2 atom within the imidazole ring, whereas it is protonated at both the Nε2 and the Nδ1 atoms in the protonated form. The blue and red colors, respectively, denote the density of positive and negative charges, and the apolar and polar surfaces are indicated by white/gray color on the molecular surfaces. In the expanded views, the location of His382 is clearly marked on the molecular surfaces, with the parentheses indicating the overall charge on this residue in the unprotonated (0) and protonated (+) forms. The ZRE duplex is displayed as a stick model, and colored green for clarity.

approximately −75° and −25°. This observation suggests that, upon protonation of His382, the αII helix not only becomes more dynamic but may also have some features resembling those of the 3_{10} helix that typically occupies the bottom left quadrant of the Ramachandran plot, with ϕ and ψ values of approximately −50° and −25°. This notion gains further credibility in light of our analysis showing that, whereas intramolecular hydrogen bonds within the the αII helix mainly occur between residues i and $i + 4$, characteristic of an ideal α-helix, in the unprotonated form of DB, protonation of His382 not only perturbs this network, but also favors the formation of hydrogen bonds between residues i and $i + 3$, which feature heavily in a 3_{10} helix (Fig. 8C).

Our thermodynamic data presented above suggest that protonation of the Nδ1 atom of His382 probably results in the disruption of a hydrogen bond between the Hε2 atom of His382 and the N7 atom of G0. To test this hypothesis using our MD simulations, we also

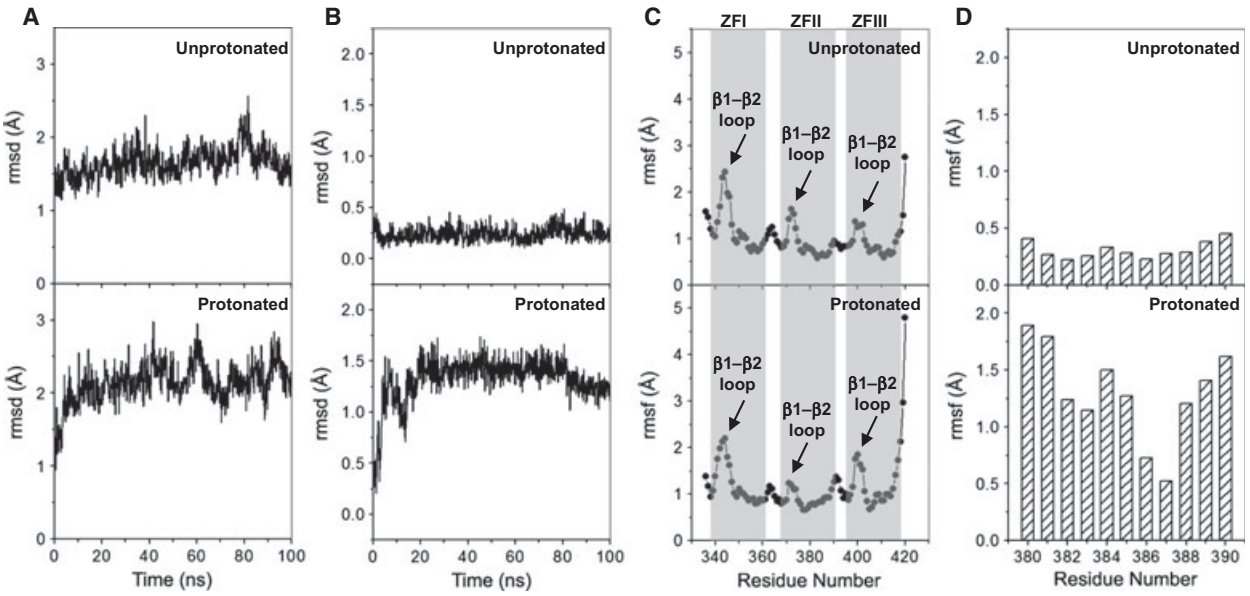

Fig. 7. Effect of protonation on the dynamics of DB of EGR1, as determined from MD analysis on the structural models of DB_WT of EGR1 containing His382 in the unprotonated and protonated forms in complex with the ZRE duplex. Note that, in the unprotonated form, His382 is protonated only at the Nε2 atom within the imidazole ring, whereas it is protonated at both the Nε2 and the Nδ1 atoms in the protonated form. (A) rmsd of backbone atoms (N, Cα, and C) within each simulated structure relative to the initial modeled structure of DB as a function of simulation time in the unprotonated (top panel) and protonated (bottom panel) forms. (B) rmsd per residue within each simulated structure relative to the initial modeled structure for the αII helix (residues 380–390) located within ZFII of DB as a function of simulation time in the unprotonated (top panel) and protonated (bottom panel) forms. (C) rmsf of backbone atoms (N, Cα, and C) averaged over the entire course of the corresponding MD trajectory of DB as a function of residue number in the unprotonated (top panel) and protonated (bottom panel) forms. Note that the vertical gray boxes denote the boundaries of residues encompassing ZFI, ZFII and ZFIII within DB. The position of the β1–β2 loop within each ZF is also indicated. (D) rmsf per residue averaged over the entire course of the corresponding MD trajectory for the αII helix (residues 380–390) located within ZFII of DB as a function of residue number in the unprotonated (top panel) and protonated (bottom panel) forms.

plotted the distance between the Hε2 atom and the N7 atom as a function of simulation time (Fig. 8D). Our analysis reveals that, whereas this distance remains constant within the unprotonated state of DB, at ~ 2 Å, throughout the 100-ns simulation cycle, it shows a fluctuation of > 4 Å after ~ 10 ns in the protonated state. This finding thus supports the notion that the hydrogen bond between the Hε2 atom of His382 and the N7 atom of G0 is less stable in the protonated form of DB. In summary, our MD simulations strongly suggest that the protonation of His382 results in marked changes associated with protein dynamics, and, in particular, results in the order–disorder transition of the αII helix. It is important to note here that, whereas our far-UV CD analysis presented above suggests that the solution pH has little effect or a negligible effect on the secondary structure and thermal stability of DB, our MD simulations have provided key insights into how protonation of His382 alters protein structure and stability at the atomic level.

pH-dependent binding to DNA appears to be a hallmark of all members of the EGR family and the related Krueppel-like factor (KLF) family

In an attempt to analyze the extent to which modulation of DNA binding through protonation of His382 in EGR1 may also be shared by other members, we generated an amino acid sequence alignment of the DBs of all known members of the human EGR family and the related KLF family (Fig. 9). It should be noted that the DBSs of all members of the EGR and KLF families are characterized by the presence of three tandem copies of C2H2-type ZFs, herein designated ZFI, ZFII, and ZFIII, which are all expected to come together to assemble into an arc-shaped architecture, so as to snugly fit into the major groove of DNA in a manner akin to the binding of EGR1 (Fig. 1A). Importantly, our analysis reveals that the DBs of all four members of the EGR family (EGR1–EGR4) are remarkably well conserved, and show sequence identity of close to 80%. However, the the DBs of EGR family

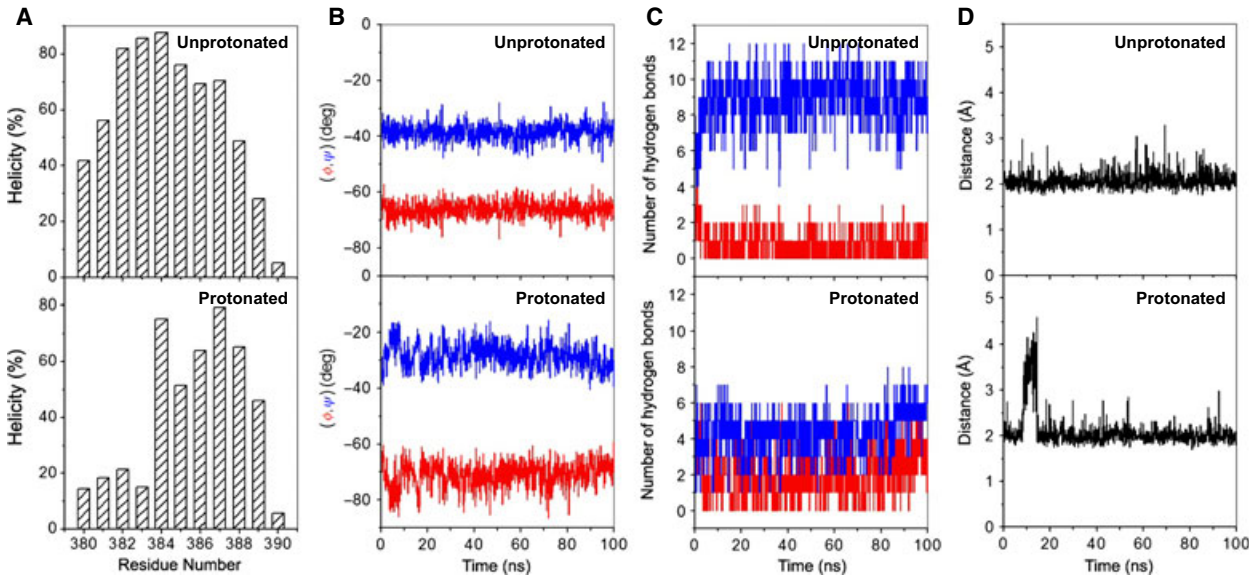

Fig. 8. Effect of protonation on the structural stability of the αII helix (residues 380–390) located within ZFII of DB of EGR1, as determined from MD analysis on the structural models of DB_WT of EGR1 containing His382 in the unprotonated and protonated forms in complex with the ZRE duplex. Note that, in the unprotonated form, His382 is protonated only at the Nε2 atom within the imidazole ring, whereas it is protonated at both the Nε2 and the Nδ1 atoms in the protonated form. (A) Helicity as a function of residue number within the αII helix ZFII in the unprotonated (top panel) and protonated (bottom panel) forms of DB. Note that helicity is defined as the percentage of time that each residue samples the α-helical conformation over the course of the simulation. (B) Dependence of backbone torsion angles ϕ (red) and ψ (blue) within the αII helix of ZFII in the unprotonated (top panel) and protonated (bottom panel) forms of DB. (C) Variation of the number of intramolecular backbone hydrogen bonds between residues *i* and (*i* + 3), characteristic of a 3_{10}-helical conformation (red), and between residues *i* and (*i* + 4), characteristic of an α-helical conformation (blue), observed within the αII helix of ZFII in the unprotonated (top panel) and protonated (bottom panel) forms of DB. (D) Distance between the Hε2 atom (the hydrogen atom directly attached to Nε2) in the imidazole ring of His382 and the N7 atom in the guanine base of G0 as a function of time in the unprotonated (top panel) and protonated (bottom panel) forms of DB. Note that G0, according to the nomenclature shown in Fig. 1B, is the central guanine of the middle trinucleotide subsite that accommodates ZFII within DB.

members share only ~ 35% sequence identity with the DBs of KLF family members (KLF1–KLF17). Accordingly, these differences at the amino acid sequence level must define the precise mechanism and differential specificity of recognition of DNA promoter elements by the EGR/KLF family members.

Notably, whereas His382 within ZFII of EGR1 is fully conserved in all other EGR family members, it is replaced by a glutamate at the structurally equivalent position within ZFII of all KLF family members. Strikingly, whereas the glutamates located at the structurally equivalent position to His382 within ZFI (Glu354) and ZFIII (Glu410) of EGR1 are fully conserved within other EGR family members, they are replaced by histidines within all KLF family members. Simply put, whereas His382 within ZFII is not conserved in KLF family members, the latter have evolved to acquire a structurally equivalent histidine within ZFI and ZFII. Accordingly, this salient observation implies that these conserved histidines are likely to be subject to protonation–deprotonation in response to changes in solution pH. On the basis of this argument, we suggest that the binding of all members of the EGR and KLF families to DNA must be tightly regulated by solution pH. Importantly, our analysis also predicts that, unlike EGR family members, KLF family members contain not one but two potential sites of protonation. Accordingly, the solution pH may play an even more intricate role in modulating the binding of KLF family members to DNA. This notion is supported by our thermodynamic data indicating that the binding of DB_HH of EGR1 to DNA shows much stronger dependence on solution pH than binding of DB_WT (Tables 1 and 3).

Conclusions

The role of EGR1 in regulating a myriad of cellular activities, ranging from cell growth and proliferation to apoptosis and oncogenic transformation, is well documented [1–4]. Our demonstration here that solution pH is likely to modulate the binding of EGR1 to

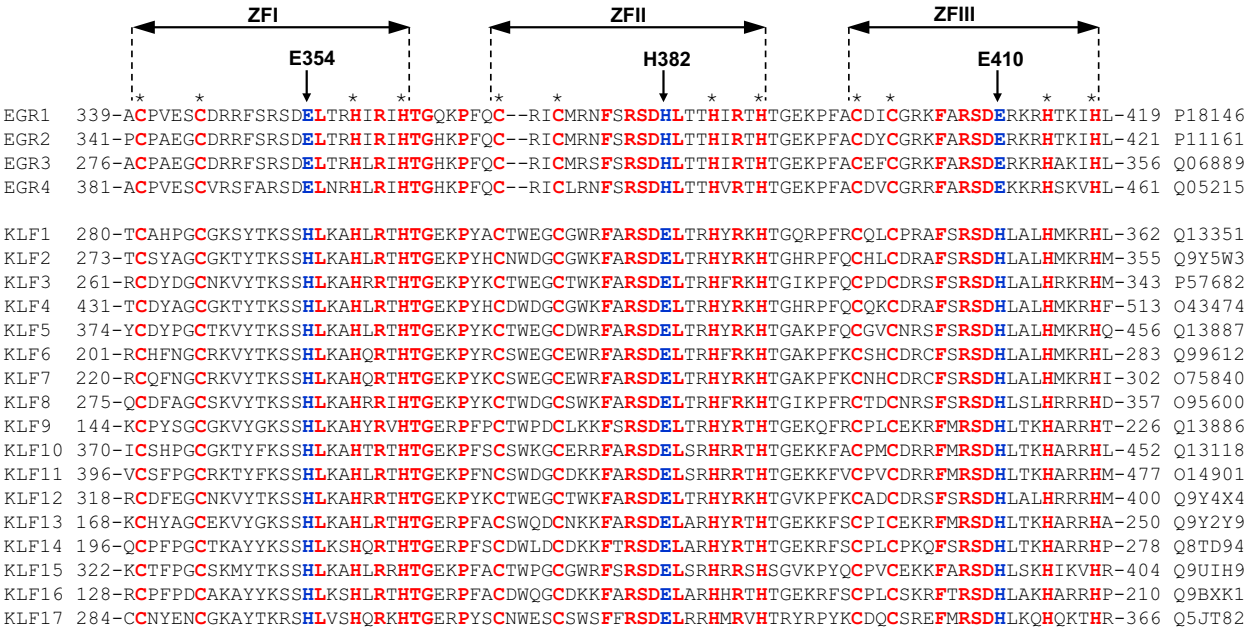

Fig. 9. Amino acid sequence alignment of DBs of all known members of the human EGR family (EGR1–EGR4) and the related human KLF family (KLF1–KLF17). Absolutely conserved residues are shown in red, nonconserved residues at structurally equivalent positions occupied by Glu354, His382 and Glu410 in EGR1 are shown in blue, and all other residues are shown in black. Each member is denoted by its acronym in the left column, and the corresponding UniProt code is provided in the right column to enable access to complete proteomic details for each member. The numerals denote the amino acid boundaries of DBs for each member. The cysteines and histidines within each of the three C2H2-type ZFs of DB, denoted ZFI, ZFII, and ZFIII, that coordinate the Zn^{2+} in a tetrahedral arrangement are marked by asterisks. The vertical arrows indicate the positions of Glu354, His382 and Glu410 in EGR1 and their structural equivalents in other DBs.

DNA, and therefore, by extension, its transcriptional activity, adds another dimension to the functional complexity of this key player in cellular signaling. Tellingly, changes in intracellular pH regulate a plethora of cellular processes, such as metabolic homeostasis and apoptosis [25]. Moreover, it is well documented that ionizable residues within proteins sense such changes, and activate a variety of proton pumps and ion transporters that, in turn, mediate extracellular transport of protons and anions to regulate intracellular pH [26–28]. Accordingly, it is tempting to speculate that changes in intracellular pH may also tightly regulate the transcriptional activity of EGR1 through modulating the ionization state of His382 located at the protein–DNA interface. Importantly, protonation–deprotonation of His382 would have important consequences for the contributions of intermolecular hydrogen bonding and van der Waals forces to the free energy available to drive this key protein–DNA interaction. It is noteworthy that the protonation–deprotonation of His382 may not necessarily require large changes, but rather may be mediated by small changes in intracellular pH. In particular, in pathological states such as metabolic acidosis or alkalosis, the transcriptional activity of EGR1 is likely to be substantially altered. This would probably have serious consequences for cellular signaling cascades that rely on EGR1 for the coupling of extracellular information in the form of hormones, neurotransmitters and growth factors to changes in gene expression of specific target proteins.

In short, our study demonstrates that the solution pH tightly modulates the binding of EGR1 to DNA by virtue of the ability of His382 to serve as a protonation–deprotonation site. Given that His382 is conserved in the structurally equivalent positions within the C2H2-type ZFs of other EGR family members and the related KLF family members, our findings have important implications for the physiological functions of these proteins. Our study suggests that this group of transcription factors may also act as sensors of intracellular pH, and thus suggests a paradigm shift regarding their molecular action.

Experimental procedures

Protein preparation

DB_WT (residues 331–430) of human EGR1 (UniProt no. P18146) was cloned into the pET30 bacterial

expression vector with an N-terminal His-tag, by the use of Novagen ligation-independent cloning technology (Novagen, Madison, WI, USA). DB_H382A, DB_H382K, DB_H382R, DB_H382E and DB_HH were generated by *de novo* DNA synthesis, courtesy of GenScript Corporation (GenScript, Piscataway, NJ, USA), and subsequently cloned into the pET30 bacterial expression vector as described for DB_WT. Additionally, a tryptophan was added at both the N-terminus and C-terminus of the wild type and mutant constructs to aid in protein characterization upon purification, because DB of EGR1 does not contain a native tryptophan. All recombinant proteins were subsequently expressed in *Escherichia coli* BL21* (DE3) (Invitrogen, Carlsbad, CA, USA), and purified on an Ni^{2+}–nitrilotriacetic acid affinity column, as described previously for other systems from our laboratory [29–31]. Briefly, bacterial cells were grown at 20 °C in Terrific Broth supplemented with 50 μM $ZnCl_2$ to an attenuance of greater than unity at 600 nm, prior to induction with 0.5 mM isopropyl thio-β-D-galactoside. The bacterial culture was further grown overnight at 20 °C, and the cells were subsequently harvested and disrupted with a Bead-Beater (Biospec, Bartlesville, OK, USA). After separation of cell debris by high-speed centrifugation (30 000 ***g*** for 30 min), the cell lysate was loaded onto an Ni^{2+}–nitrilotriacetic acid column and washed extensively with 20 mM imidazole to remove nonspecific binding of bacterial proteins to the column. The recombinant proteins were subsequently eluted with 200 mM imidazole, and dialyzed against an appropriate buffer to remove excess imidazole. The proteins were further passed through a Hiload Superdex 200 size-exclusion chromatography column coupled in line with the GE Akta FPLC system (GE Healthcare, Milwaukee, WI, USA). This final step resulted in purification of recombinant proteins to apparent homogeneity, as judged by SDS/PAGE analysis. Final yields were typically 5–10 mg of protein of apparent homogeneity per liter of bacterial culture. Protein concentration was determined with the fluorescence-based Quant-It assay (Invitrogen) and spectrophotometrically with an extinction coefficient of 12 865 $M^{-1}\cdot cm^{-1}$, calculated with the online software PROTPARAM on the ExPasy Server. The results from the two methods were in good agreement.

DNA synthesis

Fifteen-mer DNA oligonucleotides containing the ZRE consensus site (GCGTGGGCG) were obtained from Sigma Genosys (The Woodlands, TX, USA). The complete nucleotide sequences of the sense and antisense oligonucleotides constituting the ZRE duplex are shown Fig. 1B. Oligonucleotide concentrations were determined spectrophotometrically on the basis of their extinction coefficients derived from their nucleotide sequences with the online software OLIGOANALYZER 3.1 (Integrated DNA Technologies, Coralville, IA, USA). Equimolar amounts of sense and antisense oligonucleotides were mixed together and heated at 95 °C for 10 min, and then allowed to cool to room temperature to obtain dsDNA-annealed oligonucleotides (ZRE duplex).

ITC measurements

ITC experiments were performed on a TA Nano-ITC instrument (New Castle, DE, USA). Briefly, wild-type and mutant DBs of EGR1 and the ZRE dsDNA oligonucleotides were dialyzed either in 50 mM sodium acetate (for measurements conducted below pH 6) or 50 mM sodium phosphate (for measurements conducted at or above pH 6) containing 100 mM NaCl and 5 mM β-mercaptoethanol at a specified pH. All experiments were initiated by injecting 25 × 10-μL aliquots of 100 μM ZRE duplex from the syringe into the calorimetric cell containing 0.95 mL of 10–20 μM DB solution at 25 °C. The change in thermal power as a function of each injection was automatically recorded with the integrated NANOANALYZE software. The raw data were further integrated to yield binding isotherms of heat release per injection as a function of the molar ratio of ZRE duplex to DB. The heats of mixing and dilution were subtracted from the heat of binding per injection by carrying out a control experiment in which the same buffer in the calorimetric cell was titrated against the ZRE duplex in an identical manner. Control experiments with scrambled dsDNA oligonucleotides generated similar thermal power to that obtained for the buffer alone, implying that there was no nonspecific binding of DB to noncognate DNA sequences. To determine the binding constant (K_d) and the binding enthalpy (ΔH), the binding isotherms were iteratively fitted to the following built-in function by nonlinear least squares regression analysis with the integrated NANOANALYZE software:

$$q(i) = (nVP\Delta H_d/2)([1 + (L/nP) + (K_d/nP)] - \{[1 + (L/nP) + (K_d/nP)]^2 - (4L/nP)\}^{1/2}) \quad (1)$$

where $q(i)$ is the heat release ($kcal\cdot mol^{-1}$) for the ith injection, n is the binding stoichiometry, V is the effective volume of protein solution in the calorimetric cell (0.95 mL), P is the concentration of each DB in the calorimetric cell (μM), and L is the concentration of ZRE duplex added (μM). It should be noted that Eqn (1) is derived by use of the law of mass action, assuming a one-site binding model [32]. The free energy change (ΔG) upon DNA binding was calculated from the relationship:

$$\Delta G = RT \ln K_d \quad (2)$$

where R is the universal molar gas constant ($1.99\ cal\cdot mol^{-1}\cdot K^{-1}$) and T is the absolute temperature

(298 K). The entropic contribution ($T\Delta S_{obs}$) to the free energy of binding was calculated from the relationship:

$$T\Delta S = \Delta H - \Delta G \quad (3)$$

CD

CD measurements were conducted on a Jasco J-815 spectropolarimeter (Jasco, Easton, MD, USA), thermostatically controlled at 25 °C. Briefly, the wild-type and mutant DBs of EGR1 were prepared in 50 mM sodium phosphate at a specified pH ranging from 5 to 8. Experiments were conducted on 10 μM protein, and data were collected by use of a quartz cuvette with a 2-mm pathlength in the 190–260-nm wavelength range. All data were recorded with a slit bandwidth of 2 nm at a scan rate of 10 nm·min^{-1}, and normalized against reference spectra to remove the background contribution of buffer. Each spectral dataset represents an average of four scans acquired at 0.1-nm intervals. Data were converted to mean ellipticity, [θ], as a function of wavelength (λ) of electromagnetic radiation, with the equation:

$$[\theta] = [(10^5\Delta\theta)/cl]deg\ cm^2\ dmol^{-1} \quad (4)$$

where Δθ is the observed ellipticity in mdeg, c is the protein concentration (μM), and l is the cuvette pathlength (cm). For temperature scans of wild-type and mutant DBs of EGR1 to generate melting curves, the spectral intensity at a wavelength of 222 nm was monitored in the temperature range 20–100 °C at a scan rate of 1 °C·min^{-1}. It is noteworthy that the introduction of various single and double mutations did not lead to any substantial changes in the structure or stability of DB.

Molecular modeling

Molecular modeling was employed to build a structural model of DB of EGR1 in complex with the 15-mer ZRE duplex. Briefly, the structural model was built in two stages: first, the double-helical B-DNA conformation of the ZRE duplex was obtained on the basis of *de novo* modeling with 3D-DART [33]. Next, the crystal structure of DB of EGR1 in complex with a dsDNA oligonucleotide containing the ZRE consensus motif (Protein Data Bank no. 1ZAA), but with varying flanking sequences, and the *de novo* model of the ZRE duplex were used as templates in a multitemplate alignment fashion to calculate the overall structural model of the protein–DNA complex with MODELLER software, based on homology modeling [34]. A total of 100 structural models were calculated, and the structure with the lowest energy, as judged by the MODELLER Objective Function, was selected for further analysis. The structural model was rendered with RIBBONS [35], and the electrostatic surface potentials maps were generated with MOLMOL [36].

MD

MD simulations on the structural models of DB of EGR1 in the unprotonated and protonated forms with respect to His382 in complex with the ZRE duplex were performed with GROMACS software [37,38], by use of the integrated AMBER99SB-ILDN forcefield [39,40]. Briefly, the modeled structure of DB of EGR1 was subjected to GROMACS and protonated either at only the Nε2 atom (unprotonated form) or at both the Nε2 and the Nδ1 atoms (protonated form) within the imidazole ring of His382. Next, each structure was centered within a cubic box, and hydrated by use of the extended simple point charge water model [41,42], and the ionic strength of the solution was set to 100 mM with NaCl. The hydrated structures were energy-minimized with the steepest descent algorithm prior to equilibration under the *NPT* ensemble conditions, wherein the number of atoms (N), pressure (P) and temperature (T) within the system were, respectively, kept constant at ~ 50 000, 1 bar, and 300 K. The particle-mesh Ewald method was employed to compute long-range electrostatic interactions, with a 10-Å cut-off [43] and the Linear Constraint Solver (LINCS) algorithm to restrain bond lengths [44]. All MD simulations were performed under periodic boundary conditions, by use of the leap-frog integrator with a time step of 2 fs. For the final MD production runs, data were collected every 100 ps over a period of 100 ns. All simulations were run on a Linux workstation with parallel processors at the High Performance Computing facility within the Center for Computational Science of the University of Miami.

Acknowledgements

The authors are deeply indebted to M. Ahmed for many critical discussions and helpful suggestions. We thank the Sylvia Daunert Group for the use of its Jasco J-815 spectropolarimeter. This work was supported by funds from the National Institutes of Health (Grant no. R01-GM083897) and the USylvester Braman Family Breast Cancer Institute to A. Farooq. C. B. McDonald is a recipient of a postdoctoral fellowship from the National Institutes of Health (Award no. T32-CA119929).

References

1 Yan SF, Fujita T, Lu J, Okada K, Shan Zou Y, Mackman N, Pinsky DJ & Stern DM (2000) Egr-1, a master switch coordinating upregulation of divergent gene families underlying ischemic stress. *Nat Med* **6**, 1355–1361.

2 Thiel G & Cibelli G (2002) Regulation of life and death by the zinc finger transcription factor Egr-1. *J Cell Physiol* **193**, 287–292.

3 Ahmed MM (2004) Regulation of radiation-induced apoptosis by early growth response-1 gene in solid tumors. *Curr Cancer Drug Targets* **4**, 43–52.
4 Adamson ED & Mercola D (2002) Egr1 transcription factor: multiple roles in prostate tumor cell growth and survival. *Tumour Biol* **23**, 93–102.
5 Levin WJ, Press MF, Gaynor RB, Sukhatme VP, Boone TC, Reissmann PT, Figlin RA, Holmes EC, Souza LM & Slamon DJ (1995) Expression patterns of immediate early transcription factors in human non-small cell lung cancer. The Lung Cancer Study Group. *Oncogene* **11**, 1261–1269.
6 Joslin JM, Fernald AA, Tennant TR, Davis EM, Kogan SC, Anastasi J, Crispino JD & Le Beau MM (2007) Haploinsufficiency of EGR1, a candidate gene in the del(5q), leads to the development of myeloid disorders. *Blood* **110**, 719–726.
7 Huang RP, Fan Y, de Belle I, Niemeyer C, Gottardis MM, Mercola D & Adamson ED (1997) Decreased Egr-1 expression in human, mouse and rat mammary cells and tissues correlates with tumor formation. *Int J Cancer* **72**, 102–109.
8 Calogero A, Arcella A, De Gregorio G, Porcellini A, Mercola D, Liu C, Lombari V, Zani M, Giannini G, Gagliardi FM *et al*. (2001) The early growth response gene EGR-1 behaves as a suppressor gene that is down-regulated independent of ARF/Mdm2 but not p53 alterations in fresh human gliomas. *Clin Cancer Res* **7**, 2788–2796.
9 Virolle T, Adamson ED, Baron V, Birle D, Mercola D, Mustelin T & de Belle I (2001) The Egr-1 transcription factor directly activates PTEN during irradiation-induced signalling. *Nat Cell Biol* **3**, 1124–1128.
10 Krones-Herzig A, Mittal S, Yule K, Liang H, English C, Urcis R, Soni T, Adamson ED & Mercola D (2005) Early growth response 1 acts as a tumor suppressor *in vivo* and *in vitro* via regulation of p53. *Cancer Res* **65**, 5133–5143.
11 Baron V, Adamson ED, Calogero A, Ragona G & Mercola D (2006) The transcription factor Egr1 is a direct regulator of multiple tumor suppressors including TGFbeta1, PTEN, p53, and fibronectin. *Cancer Gene Ther* **13**, 115–124.
12 Thigpen AE, Cala KM, Guileyardo JM, Molberg KH, McConnell JD & Russell DW (1996) Increased expression of early growth response-1 messenger ribonucleic acid in prostatic adenocarcinoma. *J Urol* **155**, 975–981.
13 Eid MA, Kumar MV, Iczkowski KA, Bostwick DG & Tindall DJ (1998) Expression of early growth response genes in human prostate cancer. *Cancer Res* **58**, 2461–2468.
14 Baron V, De Gregorio G, Krones-Herzig A, Virolle T, Calogero A, Urcis R & Mercola D (2003) Inhibition of Egr-1 expression reverses transformation of prostate cancer cells *in vitro* and *in vivo*. *Oncogene* **22**, 4194–4204.
15 Baron V, Duss S, Rhim J & Mercola D (2003) Antisense to the early growth response-1 gene (Egr-1) inhibits prostate tumor development in TRAMP mice. *Ann N Y Acad Sci* **1002**, 197–216.
16 Virolle T, Krones-Herzig A, Baron V, De Gregorio G, Adamson ED & Mercola D (2003) Egr1 promotes growth and survival of prostate cancer cells. Identification of novel Egr1 target genes. *J Biol Chem* **278**, 11802–11810.
17 Pavletich NP & Pabo CO (1991) Zinc finger–DNA recognition: crystal structure of a Zif268–DNA complex at 2.1 A. *Science* **252**, 809–817.
18 Harris TK & Turner GJ (2002) Structural basis of perturbed pKa values of catalytic groups in enzyme active sites. *IUBMB Life* **53**, 85–98.
19 Rostkowski M, Olsson MH, Sondergaard CR & Jensen JH (2011) Graphical analysis of pH-dependent properties of proteins predicted using PROPKA. *BMC Struct Biol* **11**, 6.
20 Lumry R & Rajender S (1970) Enthalpy–entropy compensation phenomena in water solutions of proteins and small molecules: a ubiquitous property of water. *Biopolymers* **9**, 1125–1227.
21 Eftink MR, Anusiem AC & Biltonen RL (1983) Enthalpy–entropy compensation and heat capacity changes for protein–ligand interactions: general thermodynamic models and data for the binding of nucleotides to ribonuclease A. *Biochemistry* **22**, 3884–3896.
22 Cooper A, Johnson CM, Lakey JH & Nollmann M (2001) Heat does not come in different colours: entropy–enthalpy compensation, free energy windows, quantum confinement, pressure perturbation calorimetry, solvation and the multiple causes of heat capacity effects in biomolecular interactions. *Biophys Chem* **93**, 215–230.
23 Sharp K (2001) Entropy–enthalpy compensation: fact or artifact? *Protein Sci* **10**, 661–667.
24 Starikov EB & Norden B (2007) Enthalpy–entropy compensation: a phantom or something useful? *J Phys Chem B* **111**, 14431–14435.
25 Boron WF (2004) Regulation of intracellular pH. *Adv Physiol Educ* **28**, 160–179.
26 Khaled AR, Moor AN, Li A, Kim K, Ferris DK, Muegge K, Fisher RJ, Fliegel L & Durum SK (2001) Trophic factor withdrawal: p38 mitogen-activated protein kinase activates NHE1, which induces intracellular alkalinization. *Mol Cell Biol* **21**, 7545–7557.
27 Khaled AR, Reynolds DA, Young HA, Thompson CB, Muegge K & Durum SK (2001) Interleukin-3 withdrawal induces an early increase in mitochondrial

membrane potential unrelated to the Bcl-2 family. Roles of intracellular pH, ADP transport, and F(0)F (1)-ATPase. *J Biol Chem* **276**, 6453–6462.
28 Puceat M, Roche S & Vassort G (1998) Src family tyrosine kinase regulates intracellular pH in cardiomyocytes. *J Cell Biol* **141**, 1637–1646.
29 Deegan BJ, Seldeen KL, McDonald CB, Bhat V & Farooq A (2010) Binding of the ERalpha nuclear receptor to DNA is coupled to proton uptake. *Biochemistry* **49**, 5978–5988.
30 Deegan BJ, Bhat V, Seldeen KL, McDonald CB & Farooq A (2011) Genetic variations within the ERE motif modulate plasticity and energetics of binding of DNA to the ERalpha nuclear receptor. *Arch Biochem Biophys* **507**, 262–270.
31 Bhat V, Kurouski D, Olenick MB, McDonald CB, Mikles DC, Deegan BJ, Seldeen KL, Lednev IK & Farooq A (2012) Acidic pH promotes oligomerization and membrane insertion of the BclXL apoptotic repressor. *Arch Biochem Biophys* **528**, 32–44.
32 Wiseman T, Williston S, Brandts JF & Lin LN (1989) Rapid measurement of binding constants and heats of binding using a new titration calorimeter. *Anal Biochem* **179**, 131–137.
33 van Dijk M & Bonvin AM (2009) 3D-DART: a DNA structure modelling server. *Nucleic Acids Res* **37**, W235–239.
34 Marti-Renom MA, Stuart AC, Fiser A, Sanchez R, Melo F & Sali A (2000) Comparative protein structure modeling of genes and genomes. *Annu Rev Biophys Biomol Struct* **29**, 291–325.
35 Carson M (1991) Ribbons 2.0. *J Appl Crystallogr* **24**, 958–961.
36 Koradi R, Billeter M & Wuthrich K (1996) MOLMOL: a program for display and analysis of macromolecular structures. *J Mol Graph* **14**, 51–55.
37 Van Der Spoel D, Lindahl E, Hess B, Groenhof G, Mark AE & Berendsen HJ (2005) GROMACS: fast, flexible, and free. *J Comput Chem* **26**, 1701–1718.
38 Hess B (2008) GROMACS 4: algorithms for highly efficient, load-balanced, and scalable molecular simulation. *J Chem Theory Comput* **4**, 435–447.
39 Lindorff-Larsen K, Piana S, Palmo K, Maragakis P, Klepeis JL, Dror RO & Shaw DE (2010) Improved side-chain torsion potentials for the Amber ff99SB protein force field. *Proteins* **78**, 1950–1958.
40 Hornak V, Abel R, Okur A, Strockbine B, Roitberg A & Simmerling C (2006) Comparison of multiple Amber force fields and development of improved protein backbone parameters. *Proteins* **65**, 712–725.
41 Toukan K & Rahman A (1985) Molecular-dynamics study of atomic motions in water. *Phys Rev B Condens Matter* **31**, 2643–2648.
42 Berendsen HJC, Grigera JR & Straatsma TP (1987) The missing term in effective pair potentials. *J Phys Chem* **91**, 6269–6271.
43 Darden TA, York D & Pedersen L (1993) Particle mesh Ewald: an N.log(N) method for Ewald sums in large systems. *J Chem Phys* **98**, 10089–10092.
44 Hess B, Bekker H, Berendsen HJC & Fraaije JGEM (1997) LINCS: a linear constraint solver for molecular simulations. *J Comput Chem* **18**, 1463–1472.